

A Detailed Comparison of Single-Camera Light-Field PIV and Tomographic PIV

Shengxian Shi^{1*}, Junfei Ding¹, Callum Atkinson², Julio Soria^{2,3}, T. H. New⁴

1 School of Mechanical Engineering, Shanghai Jiao Tong University, 200240, Shanghai, China

2 Laboratory for Turbulence Research in Aerospace and Combustion, Department of Mechanical and Aerospace Engineering, Monash University, Melbourne, VIC 3800, Australia

3 Department of Aeronautics, King Abdulaziz University, Jeddah, Kingdom of Saudi Arabia

4 School of Mechanical and Aerospace Engineering, Nanyang Technological University, 50 Nanyang Avenue, Singapore 639798, Singapore

Abstract

This paper conducts a comprehensive study between the single-camera Light Field Particle Image Velocimetry (LF-PIV) and the multi-camera Tomographic Particle Image Velocimetry (Tomo-PIV). Simulation studies were firstly performed by using synthetic light-field and tomographic particle images, which extensively examine the difference between these two techniques by varying key parameters such as pixel to microlens ratio (PMR), light-field camera Tomo-camera pixel ratio (LTPR), particle seeding density and tomographic camera number. Simulation results indicate that the single LF-PIV can achieve accuracy consistent with that of multi-camera Tomo-PIV, but requires the use of overall greater number of pixels. Experimental studies were then conducted by simultaneously measuring low-speed jet flow with a single-camera LF-PIV and a four-camera Tomo-PIV systems. Experiments confirm that given a sufficiently high pixel resolution, a single-camera LF-PIV system can indeed deliver volumetric velocity field measurements for an equivalent field of view with a spatial resolution commensurate with those of multi-camera Tomo-PIV system, enabling accurate 3D measurements in applications where optical access is limited.

Keywords: light-field particle image velocimetry; light-field camera; single-camera volumetric PIV; tomographic PIV

*Corresponding author: kirinshi@sjtu.edu.cn (Shengxian Shi).

1 Introduction

Volumetric 3-component 3-dimensional (3C-3D) velocity measurements have long been a goal of the experimental fluid mechanics community, as it provides an important means to reveal the physics of complex flows. Through more than three decades of evolution, particle image velocimetry (PIV) has progressed from 2-component 2-dimensional (2C-2D) and 3-component 2-dimensional (3C-2D) measurements to full 3C-3D flow diagnostics (Adrian 1984, Adrian et al. 2011). One of the most highly performing and widely applied volumetric PIV techniques is the Tomographic PIV (Tomo-PIV, Elsinga et al. 2006, Scarano 2013), which possesses many attractive features when compared to other 3C-3D PIV techniques. For instance, it can handle much higher seeding density and subsequently achieve higher spatial resolution than Defocusing Digital PIV (DDPIV, Pereira et al. 2000) and digital Holographic PIV (HPIV, Hinsch 2002, Meng et al. 2004), particularly when combined with time-resolved Lagrangian particle tracking (Schanz et al. 2016), and requires relatively less cameras (typically 4~8 cameras) when compared to the Synthetic Aperture PIV (SAPIV, Belden et al. 2010), which needs 8~15 cameras to cover an equivalent measurement volume.

A significant limitation of Tomo-PIV is that it requires the use of multiple views and cameras, the arrangement of which necessitates the use of a large experimental space and multiple paths of optical accesses to the measurement area. This may be problematic for many space-constrained applications and internal industrial flows

1 where it may not be possible to have multiple optical windows or to perform in-situ
2 camera calibration. For instance, applications such as blade tip leakage and secondary
3 passage flow in gas turbines, which are the key sources of the reduced efficiency of
4 turbines and compressors and can significantly impact on blade-life. Driven by the
5 significant pressure difference across these blades, such flows are highly three-
6 dimensional and quantitative measurements are further complicated by the small
7 clearances between the blade tips and casings (e.g. typically 1~2% of blade span).
8 Accurate characterisation of such flows has long been a challenge for experimental
9 research in gas turbines and only very limited 2C-2D or 3C-2D flow measurements
10 have been successfully performed (Wernet et al. 2005, Palafox et al. 2008). As such,
11 single camera based volumetric flow diagnostic techniques with large measurable
12 volume and high spatial resolution are highly desirable for these space-constrained
13 applications.

14 One such technique is the single camera based light-field particle image velocimetry
15 (shorted as LF-PIV hereafter) (Ding et al. 2015, Fahringer et al. 2015, Shi et al. 2016,
16 Shi et al. 2017, [Xu et al. 2017](#), [Li et al. 2017](#)). As the name implies, LF-PIV relies on
17 light-field photography to capture 3D information of tracer particles. Unlike SAPIV
18 which employs a camera array to record the light-field of particle images, LF-PIV
19 achieves similar functionality by using a light-field camera, which combines a high
20 resolution micro-lens array (MLA) with a CCD/CMOS sensor. Although LF-PIV has
21 been successfully applied to cylinder wake and jet flow measurements, a
22 comprehensive comparison between the performance of LF-PIV and the more widely
23 used Tomo-PIV has not been reported. In particular, it will be instructive to observe
24 how measurement uncertainty will differ between LF-PIV and Tomo-PIV when the

1 number of cameras used by Tomo-PIV varies. Furthermore, with the ever increasing
2 pixel resolution of digital image sensor technology, it will be worthwhile to predict the
3 LTPR at which LF-PIV is able to achieve equivalent accuracy in the x-, y- and z-
4 direction than Tomo-PIV.
5
6
7

8
9
10
11 To address these questions, the present study uses a series of synthetic light-field and
12 tomographic particle images to investigate the effects of Tomo-PIV camera number and
13 the pixel resolution ratio between light-field and Tomo-PIV cameras on the accuracy of
14 the reconstructed particle distributions and associated velocity. In addition, a direct
15 experimental comparison between LF-PIV and Tomo-PIV was conducted on a jet
16 facility to better quantify the practical challenges and differences between these two
17 techniques. In the following sections, information on the synthetic image generation
18 and detailed simulation studies will be provided, followed by detailed descriptions on
19 the experimental setup and the flow reconstruction results.
20
21
22
23
24
25
26
27
28
29
30
31
32
33
34
35

36 **2 Numerical Analysis with Synthetic Particle Images**

37
38 Before delving into a detailed comparison of LF-PIV and Tomo-PIV, it is important
39 to identify the key factors that affect the measurement accuracy of these two
40 techniques. In the case of Tomo-PIV, it is known that the performance is strongly
41 affected by the number of cameras and the seeding density (Elsinga et al. 2006,
42 Atkinson and Soria 2009). For LF-PIV the identification of key performance
43 parameters is not as straightforward. **In light-field camera (Ng et al. 2005)**, the MLA
44 is positioned one focal length away from the CCD/CMOS sensor, which ensures the
45 highest available angular resolution (Fig. 1a). In focused light-field camera (Fig. 1b),
46 the distance between the MLA and CCD/CMOS sensor is variable and different levels
47
48
49
50
51
52
53
54
55
56
57
58
59
60
61
62
63
64
65

of spatial resolution (resolution in each refocused slice) can be achieved by sacrificing angular resolution (Georgiev et al. 2006, Lumsdaine et al. 2009).

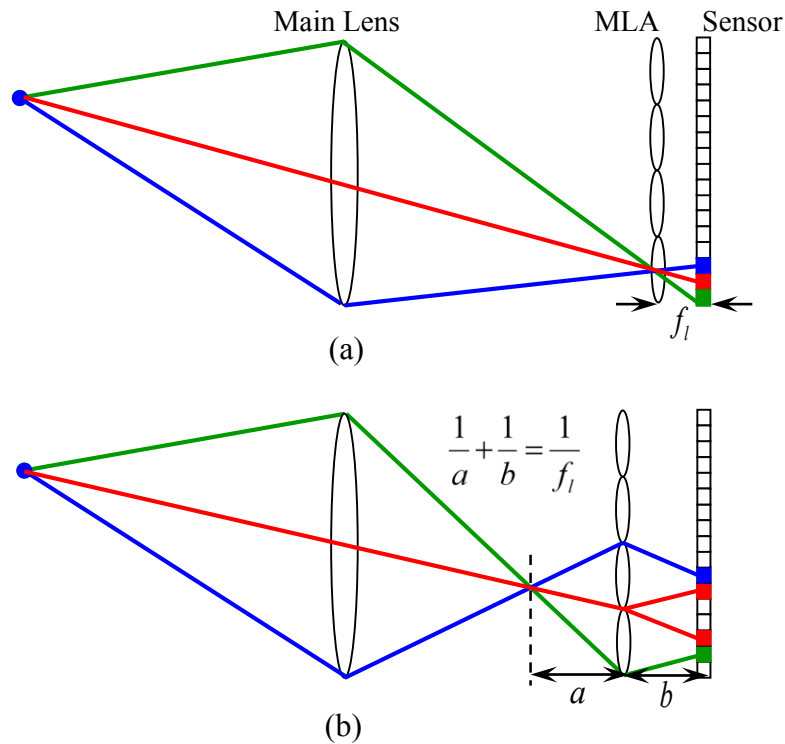


Fig. 1 Schematics of light field imaging techniques based on
 (a) light-field camera and (b) focused light-field camera
 (colour only in electronic version)

For volumetric velocity measurements, higher angular resolution is preferred over the in-plane spatial resolution as it leads to a greater information about particle displacement in the direction normal to the imaging plane. Hence, current LF-PIV techniques all made use of light-field cameras (Ding et al. 2015, Fahringer et al. 2015, Shi et al. 2017). Previous studies indicate that the performance of LF-PIV is mostly affected by the pixel-microlens ratio (PMR) as angular resolution is determined by number of pixels beneath each lenslet. In addition, higher MLA resolution can tolerate higher seeding density (Shi et al. 2016). As such, it is

1 preferable for LF-PIV to achieve as high a pixel resolution as possible, so as to
 2 produce high angular resolution (large PMR) as well as high spatial resolution (high
 3 MLA resolution). Therefore, PMR is the key factor that affects the performance of
 4 LF-PIV. When comparing LF-PIV and Tomo-PIV, it is important to consider the
 5 number of pixels required in LF-PIV compared to the total number of pixels that are
 6 employed in a multi-camera Tomo-PIV experiment. To characterise this, we defined
 7 a pixel ratio between light-field and Tomo-system (Light-field camera Tomo-
 8 cameras pixel ratio, $LTPR = \frac{(p_x \times p_y)_{LF-PIV}}{(p_x \times p_y \times N_c)_{Tomo-PIV}}$), which if we consider camera
 9 cost in terms of dollars per pixels can be taken as representative of the comparative
 10 cost of these two experimental approaches. Finally, it is known that the multi-camera
 11 Tomo-PIV system can reconstruct higher density seeding particles than the single-
 12 camera LF-PIV technique (Scarano 2013, Fahringer et al. 2015, Shi et al. 2016, Shi
 13 et al. 2017). Although the same physical seeding density (particle/mm³) could be
 14 used when performing simulation studies between LF-PIV and Tomo-PIV, tests
 15 completed in this section are based on synthetic images that feature the most
 16 favourable seeding density of each technique. In such way, both LF-PIV and Tomo-
 17 PIV can fully demonstrate their potentials, consistent with each experiment being
 18 individually optimised for a given field of view.

19 Based on the above analysis, comparative studies in this section were performed for
 20 the two techniques by varying key parameters such as the number of Tomo-PIV
 21 cameras, PMR and LTPR. For such purposes, a series of synthetic light field PIV
 22 images and Tomo-PIV images were generated by using data from a direct numerical
 23 simulation of an incompressible jet (Fig. 2a). The Reynolds number of the DNS was

2500, corresponding to a circular nozzle diameter of $D = 40\text{mm}$ and a jet exit velocity of 0.13 (dimensionless). Synthetic PIV images were generated for a measurement volume located ($x=0.5D$, $y=0.5D$, $z=1D$) from the nozzle exit (Fig. 2b). It should be noted that, in order to reduce the computational load without losing generality, relatively low-resolution synthetic Tomo-PIV cameras and light-field cameras are constructed in this section.

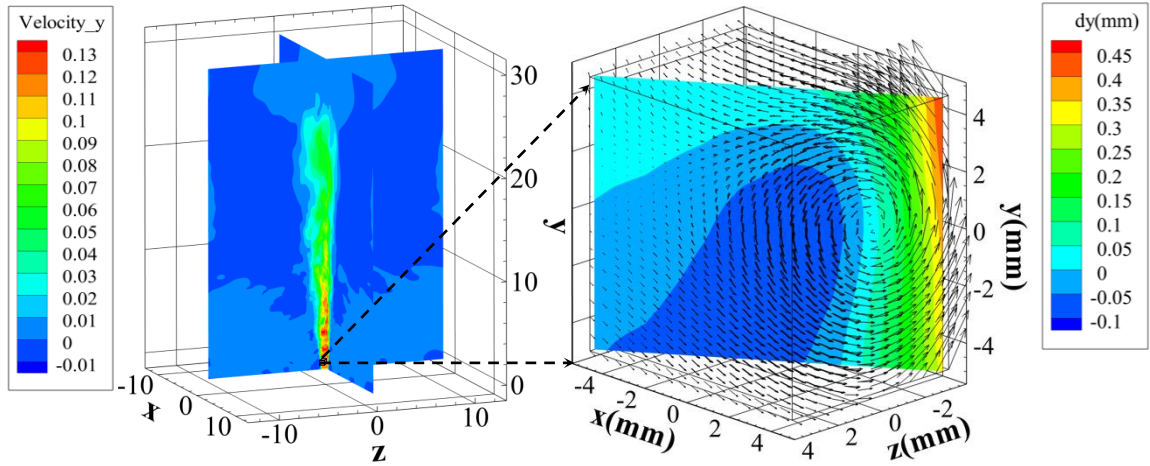


Fig. 2 (a) Overview of the DNS jet flow field; (b) Synthetic measurement volume

2.1 Generation of Synthetic Light-Field particle images

To generate synthetic light-field particle images the two-plane parameterisation of the 4D plenoptic function is used in this study (Levoy et al. 1996). Figure 3 illustrates the basic ray tracing process for generating the synthetic images. Definition of the parameters in the figure are: S_o is the object distance; S_i is the image distance; f_m is the focal length of the main lens; f_l is the focal length of the microlens; p_m is the aperture of the main lens; p_l is the microlens pitch; p_p is the pixel pitch; S_y is the coordinate of lenslet centre. Linear optics was used to calculate the spatial location of each ray during its propagation from tracer particles to the image sensor. For example, for a tracer particle located at dy above the optical axis and dz away from the focal

plane, the propagation of its scattered rays can be traced from the main lens, through the MLA and finally to the image sensor by using equations detailed in Georgiev et al. (2003) and Shi et al. (2016).

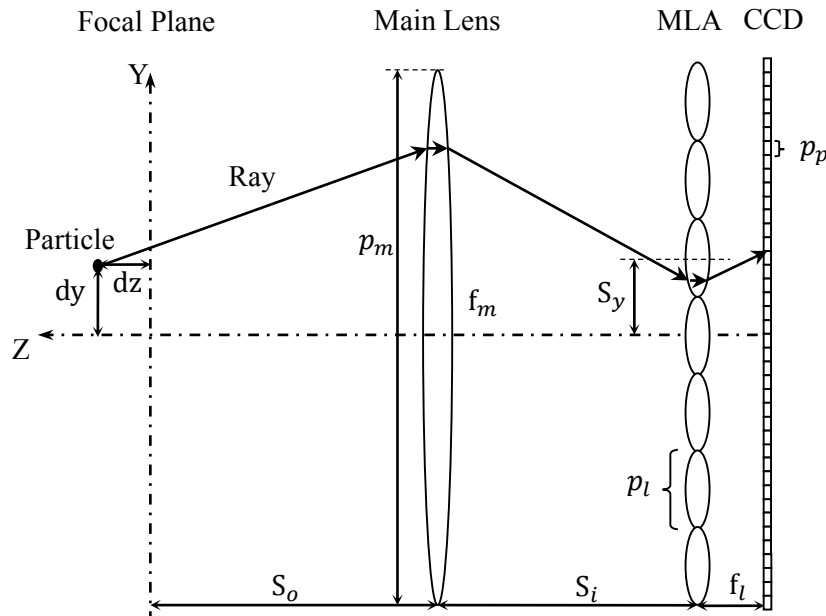


Fig. 3 Schematic of synthetic light-field particle image generation (1D model)

In this section, the synthetic light-field camera is arranged in a way that its sensor plane is parallel to the jet direction (x-y plane in Fig. 2) and its optical axis is along the z-direction (see Fig. 2). To generate the first frame of the synthetic light-field particle image, a set of random particle coordinates are generated. From each particle, five million rays are simulated spanning the aperture of the main lens and the locations where these rays hit the image sensor are calculated according to Eq. 1~5. Pixel intensities of the synthetic light-field particle image are calculated based on the number of rays received by each pixel, and are normalised to the range of 0~255. After that, these random particles are shifted according to the DNS flow with a given time interval such that the maximum imaged particle displacement complies the one-

1 quarter rule for the first pass of cross-correlation process. The ray tracing process is
2 then repeated to generate the second frame of the light field particle image.
3
4

5
6
7 To investigate the effects of PMR and LTPR on the performance of LF-PIV, two light-
8 field camera size (e.g. 800×800 pixel² and 1600×1600 pixel²) with three different
9 PMR (e.g. PMR=7, 14, 28) were simulated. Note that the hexagonal lenslet was
10 simulated to achieve a better resolution (Shi et al. 2016). In addition, one Tomo-
11 camera size (e.g. 160×160 pixel) with three different configurations (e.g. Tomo-
12 camera number $N_c=4, 6, 8$) were simulated, which results in six sets of LTPR cases
13 (e.g. LTPR=3.13, 4.17, 6.25, 12.5, 16.67 and 25). When constructing the artificial light
14 field cameras, the general principle of f-number matching between the main lens and
15 microlens was applied to maximise resolution (Ng et al. 2005). With a given pixel
16 pitch, for example, the pixel size is set as 0.015mm for the low LTPR case (see Table
17 1). When PMR varies, it changes the lenslet size and hence the focal length of the
18 lenslet needs to be adjusted accordingly in order to maintain the same f-number as the
19 main lens. To illustrate these relationships, schematics of relative geometric
20 configurations of the different synthetic light-field cameras under consideration are
21 shown in Fig. 4. For all synthetic light-field images, particle density is set to 0.5
22 particle per microlens (ppm) which was determined as the optimal density from our
23 pervious study (Shi et al. 2016). An example of a synthetic light-field particle image
24 is shown in Fig. 5a, b and c. Detailed information on parameters used in synthetic
25 particle image generation are listed in Table 1. Note that these parameters are purely
26 for theoretical analysis, and the possibility of manufacturing such light-field cameras
27 are not considered here.
28
29
30
31
32
33
34
35
36
37
38
39
40
41
42
43
44
45
46
47
48
49
50
51
52
53
54
55
56
57
58
59
60
61
62
63
64
65

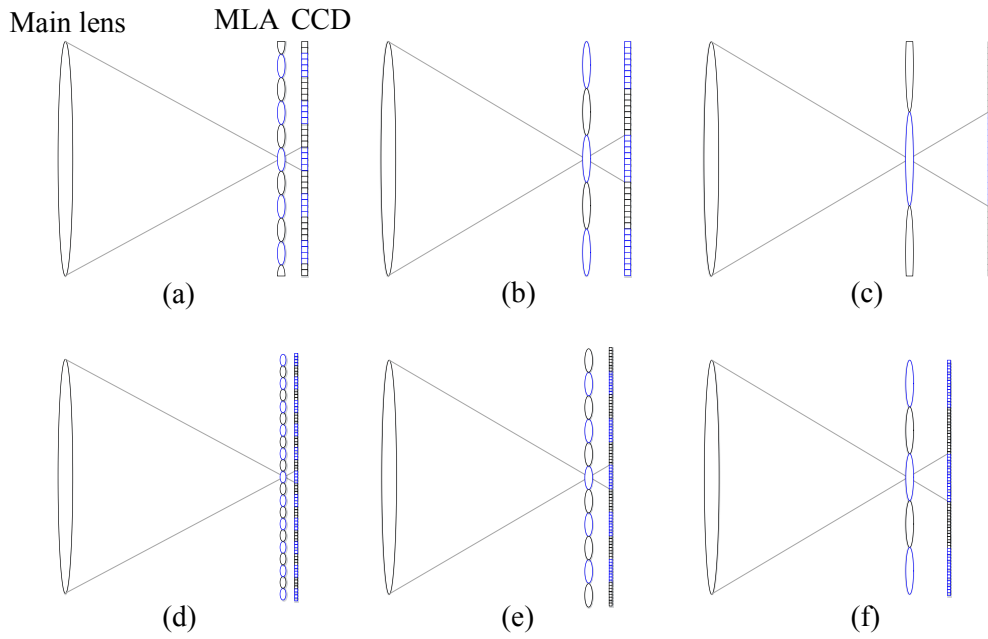


Fig. 4 Schematics of synthetic light-field camera configurations for:

(a) PMR=7, LTPR=3.13, 4.17, 6.25; (b) PMR=14, LTPR=3.13, 4.17, 6.25;

(c) PMR=28, LTPR=3.13, 4.17, 6.25; (d) PMR=7, LTPR=12.5, 16.67, 25;

(e) PMR=14, LTPR=12.5, 16.67, 25; (f) PMR=28, LTPR=12.5, 16.67, 25;

(Note that the separation between MLA and CCD varies due to the variation of MLA focal length, which is caused by different PMR)

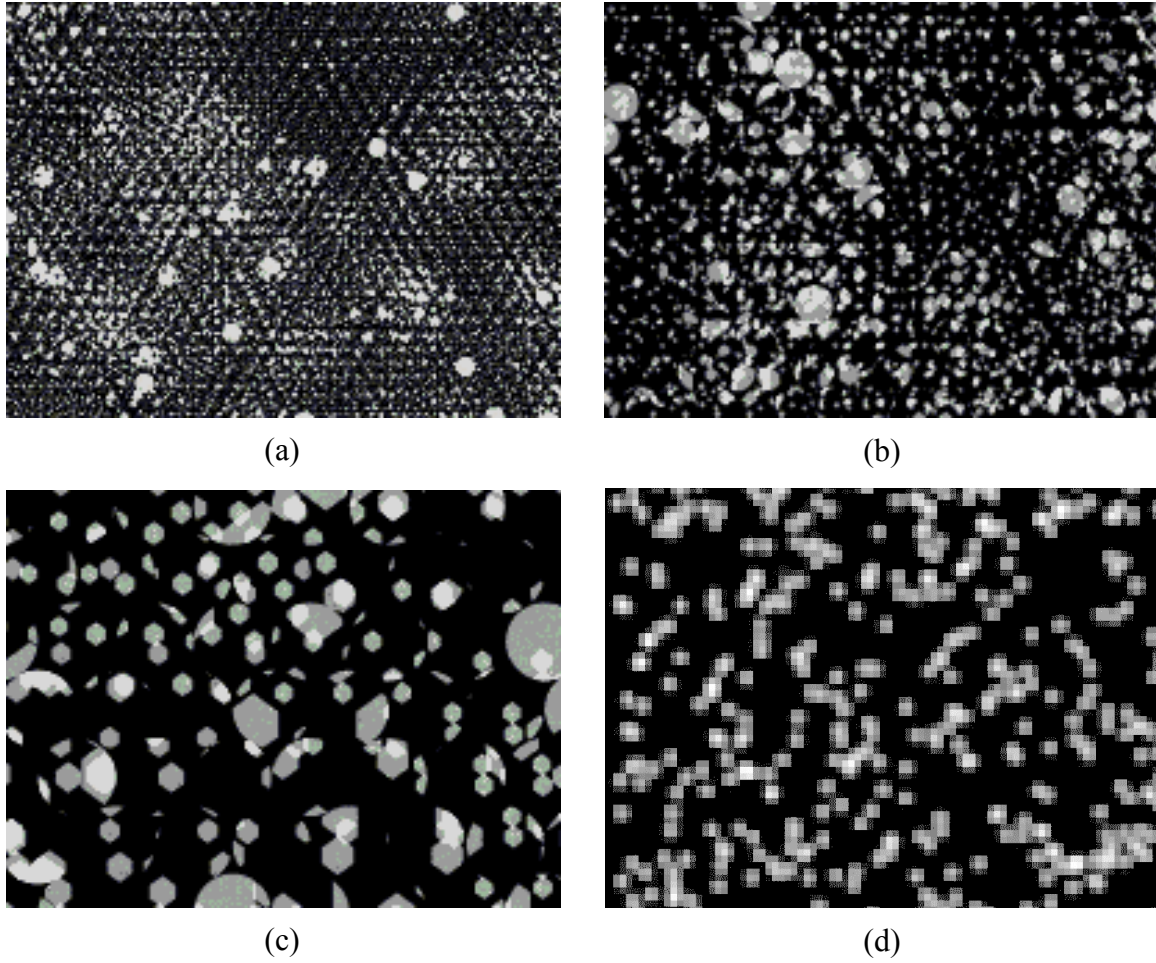


Fig. 5 Example of synthetic particle images (a) LF-PIV (LTPR=3.13, 4.17, 6.25, PMR=7, 0.5ppm); (b) LF-PIV (LTPR=3.13, 4.17, 6.25, PMR=14, 0.5ppm); (c) LF-PIV (LTPR=3.13, 4.17, 6.25, PMR=28, 0.5ppm); (d) Tomo-PIV (0.05ppm)

Table 1 Key parameters used for synthetic image generation (note that the low LTPR and high LTPR each corresponds to only one type of light-field camera resolution, e.g. 800×800 and 1600×1600. The six sets of LTPR cases are simply a results of different Tomo-camera number)

| | | LF-PIV | | | | | | Tomo-PIV | |
|--|-----|-------------------------|--------|--------|-----------------|---------|--------|---------------|------|
| Camera Number | | 1 | | | | | | $N_c = 4,6,8$ | |
| LTPR | | Low | | | High | | | - | |
| | | 6.25, 4.17, 3.13 | | | 25, 16.67, 12.5 | | | | |
| Pixel resolution of each camera | | 800×800 | | | 1600×1600 | | | 160×160 | |
| Field of View | | 12×12×10mm ³ | | | | | | | |
| p_p(mm) | | 0.015 | | | 0.0075 | | | 0.075 | |
| PMR | | 7 | 14 | 28 | 7 | 14 | 28 | - | |
| MLA resolution | | 114×132 | 57×66 | 29×33 | 228×264 | 114×132 | 57×66 | - | |
| p_l(mm) | | 0.105 | 0.210 | 0.420 | 0.0525 | 0.105 | 0.210 | - | |
| Particle density | ppm | 0.5 | | | | | | - | - |
| | ppp | 0.0118 | 0.0029 | 0.0007 | 0.0118 | 0.0029 | 0.0007 | 0.05 | 0.1 |
| Particles number | | 7524 | 1881 | 470 | 30096 | 7524 | 1881 | 1280 | 2560 |

2.2 Generation of Synthetic Tomographic particle images

Synthetic Tomographic particle image are generated for an array of cameras of equally spaced around the cubic reconstruction volume in the x-z plane with camera numbers ranging from 4, 6 and 8 (Fig. 6). The projection of 3D tracer particles to 2D image plane is calculated using a pinhole camera model (Tsai 1986) with a focal length of

85mm. The image distance and object distance are 93.4mm, 946.5mm respectively, which results in a magnification factor of 0.075 mm/pixel. A set of random particles are generated in the measurement volume, and their projections in each camera sensor are calculated by the camera matrix, which gives the image coordinate of the particle image centre. Subsequently, a Gaussian distribution is applied to the calculated image coordinate to generate a particle image with a diameter around 3 pixels. Applying this process to each camera produces the first frame of synthetic Tomographic particle images. To produce the second frame of the particle image set, the random particles are shifted to a distance calculated by the DNS flow with a given time interval so that the maximum particle image displacement corresponds to one quarter of the initial interrogation window size. These particles are then projected to each camera sensor in a similar fashion as generating the first frame of particle images. An example of synthetic Tomographic particle image is shown in Fig. 5d.

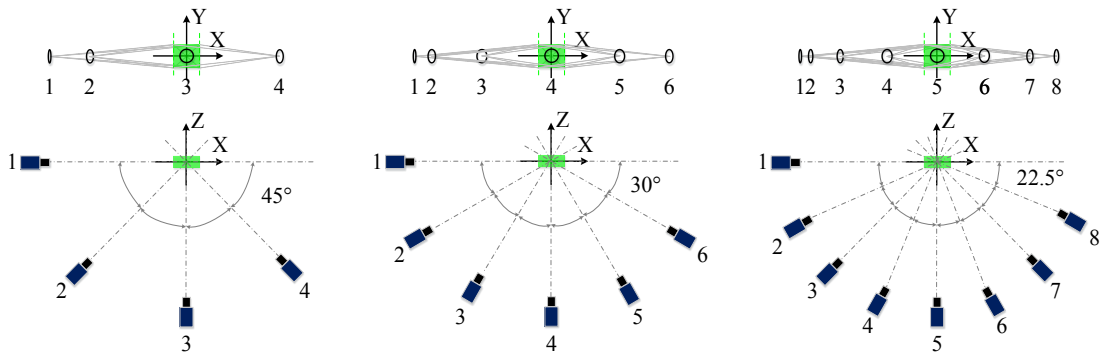


Fig. 6 Camera configurations used for synthetic Tomographic particle image generation

2.3 Simulation Results

To conduct the simulation tests, synthetic light-field and tomographic particle image pairs are firstly reconstructed by the DRT-MART (Shi et al. 2017) and MLOS-SMART (Atkinson and Soria 2009) algorithms, respectively. Instead of using 1:1

1 pixel voxel ratio, which is normally the case for Tomo-PIV, light-field particle image
2 reconstruction employs a different pixel voxel ratio in x-, y- and z-directions. This is
3
4 mainly due to the elongation effect of the reconstructed particles, especially in z-
5 direction. Previous studies demonstrate that the pixel voxel ratio of 2:2:10 in x-, y-
6 and z-direction achieves a good balance between reconstruction accuracy and
7 computational cost (Shi et al. 2017). After particle image reconstruction,
8 instantaneous velocity fields are then calculated with a two-pass, three-dimensional
9 multi-grid cross correlation method (Soria, 1996), with an overlapping ratio of 0.75.
10 While the first interrogation window size is chosen according to the one-quarter rule,
11 the final interrogation window size is determined such that there are 7~10 particles on
12 average in each window. Incorrect velocity vectors are detected by a 3×3×3 median
13 filter (Westerweel and Scarano 2005), only valid vectors were considered in the
14 subsequent analysis. Detailed information on the reconstruction and cross-correlation
15 parameters used for different test cases are listed in Table 2 below. Considering the
16 extensive computational cost required by DRT-MART and MLOS-SMART
17 reconstruction as well as three-dimensional cross correlation, all calculations are
18 accelerated by GPU parallel processing via a NVIDIA TITAN X GPU unit.
19
20
21
22
23
24
25
26
27
28
29
30
31
32
33
34
35
36
37
38
39
40
41
42
43
44
45
46
47
48
49
50
51
52
53
54
55
56
57
58
59
60
61
62
63
64
65

Table 2 Reconstruction and interrogation parameters used for synthetic image processing

| | | LF-PIV | | | | | | Tomo-PIV | |
|---|----|------------------|------------------|------------------|-------------------|------------------|------------------|-------------------|------------------|
| LTPR | | low | | | high | | | - | |
| | | 6.25, 4.17, 3.13 | | | 25, 16.67, 12.5 | | | | |
| PMR | | 7 | 14 | 28 | 7 | 14 | 28 | ppp=0.05 | ppp=0.1 |
| Reconstruction | | DRT-MART | | | | | | MLOS-SMART | |
| Iteration number | | 400 | | | | | | 40 | |
| Pixel voxel ratio | | 2:2:10 | | | | | | 1:1:1 | |
| Reconstruction Volume (voxel) | | 400×400×67 | | | 800×800×134 | | | 160×160×133 | |
| Voxel size (mm) | | 0.03×0.03×0.15 | | | 0.015×0.015×0.075 | | | 0.075×0.075×0.075 | |
| 1st window (voxel) | x- | 80 | 160 | 320 | 80 | 160 | 320 | 64 | 32 |
| | y- | 80 | 160 | 320 | 80 | 160 | 320 | 64 | 32 |
| | z- | 16 | 32 | 64 | 16 | 32 | 64 | 64 | 32 |
| 2nd window (voxel) | x- | 40 | 80 | 160 | 40 | 80 | 160 | 32 | 16 |
| | y- | 40 | 80 | 160 | 40 | 80 | 160 | 32 | 16 |
| | z- | 8 | 16 | 32 | 8 | 16 | 32 | 32 | 16 |
| 2nd window (mm³) | | 1.2 ³ | 2.4 ³ | 4.8 ³ | 0.6 ³ | 1.2 ³ | 2.4 ³ | 2.4 ³ | 1.2 ³ |

To reveal the influences of LTPR, PMR and particle density on the performance of LF-PIV and Tomo-PIV, accuracy of the reconstructed particle position is analysed for the two techniques. As the reconstructed particles are elongated in the z-direction for both techniques, the centre coordinates are calculated by using the peak centroid method instead of Gaussian peak fitting. By comparing the reconstructed particle centre with its ground truth, the probability density function (PDF) of the reconstruction errors in x-, y- and z-directions are plotted in Fig. 7 for all tested cases.

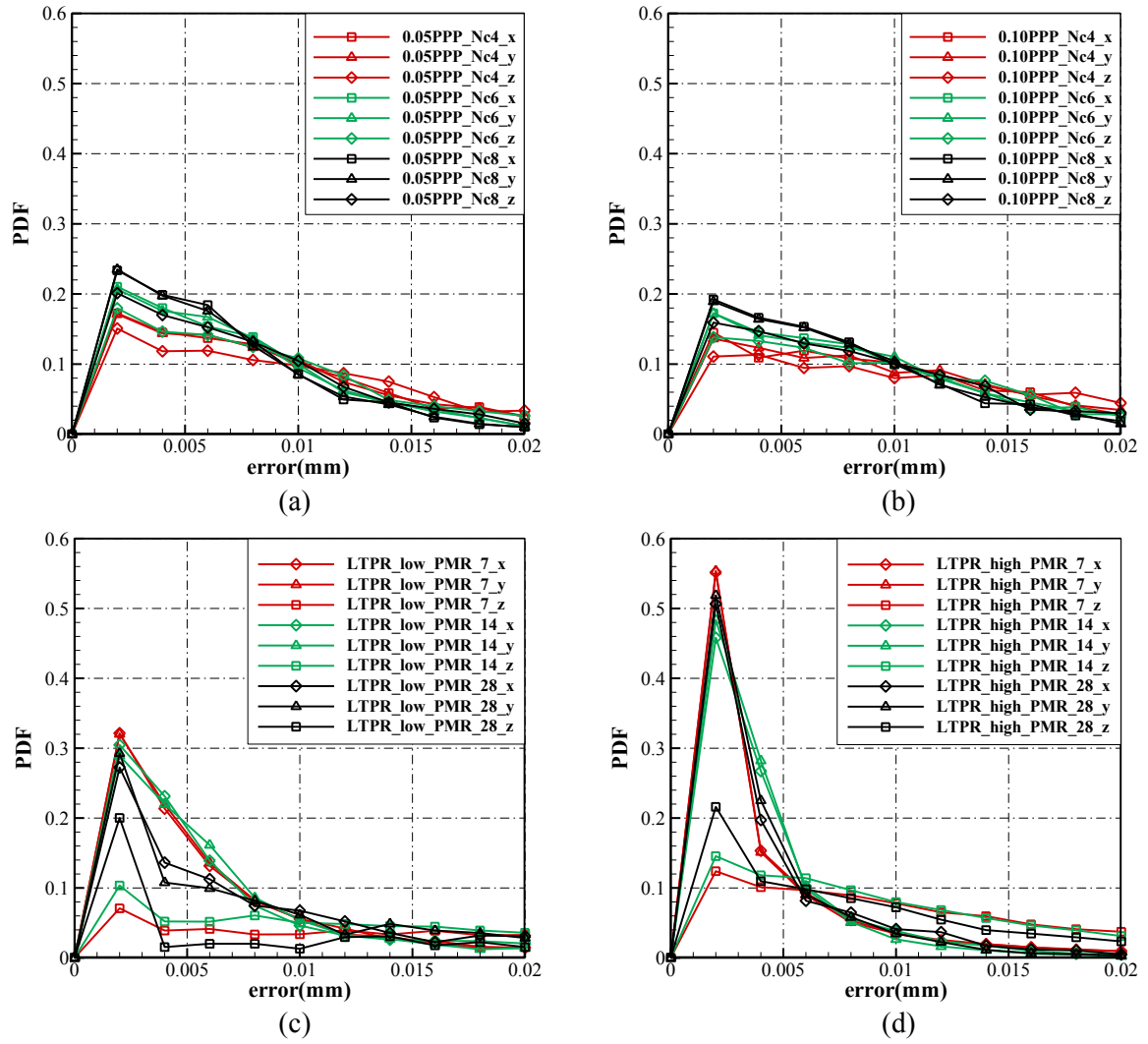


Fig. 7 Particle centre reconstruction errors of the reconstructed particle position: (a) Tomo-PIV, 0.05PPP; (b) Tomo-PIV, 0.10PPP; (c) LF-PIV, low LTPR; (d) LF-PIV, high LTPR

Figures 7a and 7b present the particle centre reconstruction errors for Tomo-PIV, which show that the reconstruction accuracy increases with an increase in camera number, but decreases with an increase in particle density. Such observations are in line with previous studies which demonstrated that more viewing angles and less seeding particles would help to mitigate the elongation effects, as well as reducing “ghost particles”, both of which contribute to a better reconstruction accuracy (Elsinga et al. 2006, Scarano 2013). On the other hand, the reconstruction accuracy of LF-PIV

1 is strongly affected by the camera resolution (or LTPR). As shown in Figs. 7c and 7d,
2 doubling the light-field camera pixel resolution would nearly double the particle centre
3 reconstruction accuracy in both x-and y-directions. For the z-direction reconstruction
4 accuracy, although it is primarily governed by the PMR, as already been proven that
5 the depth resolution is highly dependent upon the number of pixels beneath each
6 lenslet (Shi et al. 2016), it is also slightly affected by the LTPR. As shown in Fig. 7d,
7 higher LTPR clearly degrades the reconstruction error with a larger magnitude (i.e.
8 Error >0.004 mm) for all current PMR cases. This is because that, for the same PMR,
9 higher LTPR would effectively increase the MLA resolution (e.g. PMR=7, Fig. 4a and
10 4d). With higher MLA resolution, a small particle displacement in z-direction will
11 result in light rays been captured by more lenslet and more pixels, which in return will
12 help to better resolve the particle location during the reconstruction process. Details
13 of which can be found in Shi et al. (2016) (especially refer to Fig. 9 in the reference).
14 Cross comparing the results shown in Figs. 7a and 7c, it would suggest that LF-PIV is
15 likely to achieve similar accuracy as Tomo-PIV at low LTPR, PMR28 test case.
16
17
18
19
20
21
22
23
24
25
26
27
28
29
30
31
32
33
34
35
36
37
38

39 To compare the performance of these two techniques further, the calculated
40 instantaneous velocity vectors are compared with the original DNS velocity field,
41 which is spatially filtered to match the final interrogation window size. The RMS
42 errors for each velocity component are plotted in Fig. 8. Starting with the LF-PIV
43 simulation results first (Fig. 8a), for the low-resolution light-field camera (LTPR=3.13,
44 4.17, 6.25), the measurement error increases with PMR, although higher PMR offers
45 better depth resolution (Shi et al. 2016). However, for a given number of pixels, an
46 increasing in PMR can only be achieved by increasing the physical dimension of each
47 lenslet, which effectively reduces the overall number of microlens (decreased MLA
48
49
50
51
52
53
54
55
56
57
58
59
60
61
62
63
64
65

1 resolution). As a result, it leads to a reduction in the effective particle density, and
2 hence limits the final interrogation window size (Table 1). For the higher resolution
3 light-field camera (LTPR=12.5, 16.67, 25), as the MLA resolution is nearly doubled
4 (doubling the seeding density), the overall measurement error is greatly reduced for
5 x-, y- and z-direction velocity components (u, v and w respectively). This is
6 particularly true for the PMR=14 case, which achieves the best balance between depth
7 resolution (PMR) and particle density (MLA resolution), and produces the lowest
8 RMS error for the w-velocity component (around 0.15 pixels).
9

10 Fig. 8b shows the variation of RMS error with the number of cameras used in Tomo-
11 PIV. In general, increasing the number of cameras from 4 to 8 gradually improves the
12 measurement accuracy as shown by (Elsinga et a. 2006, Atkinson and Soria 2009),
13 especially for the v-velocity component. This is due to the improved reconstruction
14 quality in the y-direction, which is parallel to the image planes of these cameras.
15 However, possibly due to the increased ghost particles when particle density is too
16 high, the measurement error for PPP=0.1 case is slightly higher than the PPP=0.05
17 case (Elsinga et al. 2006, Scarano 2013). Note that single camera LF-PIV does not
18 suffer from the ghost particle reconstruction problem according to our previous studies
19 (Shi et al. 2017). Comparing the results between LF-PIV and Tomo-PIV, it is clear
20 that the measurement accuracy of single camera LF-PIV is comparable with the four-
21 camera Tomo-PIV system at a relatively low pixel resolution ratio (e.g. LTPR=3.13,
22 4.17, 6.25, PMR=7), which matches well with the observations made with Figs. 8a
23 and 8c. LF-PIV can achieve accuracy equal to or higher than Tomo-PIV for the same
24 field of view as the number of pixels continues to increase beyond that of Tomo-PIV
25 and a greater number of microlenses are used (e.g. PMR=14; LTPR>=25, for four-
26
27
28
29
30
31
32
33
34
35
36
37
38
39
40
41
42
43
44
45
46
47
48
49
50
51
52
53
54
55
56
57
58
59
60
61
62
63
64
65

camera Tomo-PIV; $LTPR \geq 16.67$, for six-camera Tomo-PIV; $LTPR \geq 12.5$, for eight-camera Tomo-PIV).

In addition to performance analysis, the computational times that the two techniques spent on particle reconstruction are compared based on current state-of-the-art hardware (NVIDIA TITAN X GPU). Note that the computational times are normalized by the reconstruction cost of the four-camera Tomo-PIV. In general, LF-PIV would take significantly longer computational time as compared to Tomo-PIV. This is due to the relationship between the voxel and the pixel in LF-PIV not based on a one-to-one mapping (which is the case in Tomo-PIV), and hence there are more non-zero pixels that need to be taken into consideration during the reconstruction stage in LF-PIV. Specifically, the reconstruction time of LF-PIV varies significantly with PMR and LTPR. Take for instance, the longest reconstruction time is incurred for PMR=7 case. As a matter of fact, a lower PMR means a smaller lenslet (Fig. 4), which effectively results in higher particle number for the same given ppm (Table 1, Figs. 5a, 5b and 5c). On the other hand, although the PMR=28 case has the lowest particle number for the same LTPR (Table 1), a non-zero voxel would affect almost all of the 28×28 pixels beneath each affected lenslet. Therefore, the total number of pixels involved in reconstruction calculation is actually larger than that of PMR=14.

Table 3 LF-PIV and Tomo-PIV reconstruction times for different PMR and particle density

| Reconstruction time | | | | | |
|---------------------|--------------------------|-------------------------|----------|-------------------------------|-------------------------------|
| LF-PIV | | | Tomo-PIV | | |
| | LTPR=6.25, 4.17, 3.13 | LTPR=25, 16.67, 12.5 | | Particle density= 0.05 PPP | Particle density= 0.10 PPP |

| | | | | | |
|--------|---------|---------|------|--------|--------|
| PMR=7 | 55.9811 | 1269.4 | Nc=4 | 1 | 1.0093 |
| PMR=14 | 3.7750 | 15.2940 | Nc=6 | 1.1405 | 1.1550 |
| PMR=28 | 7.2170 | 55.2826 | Nc=8 | 1.3690 | 1.3744 |

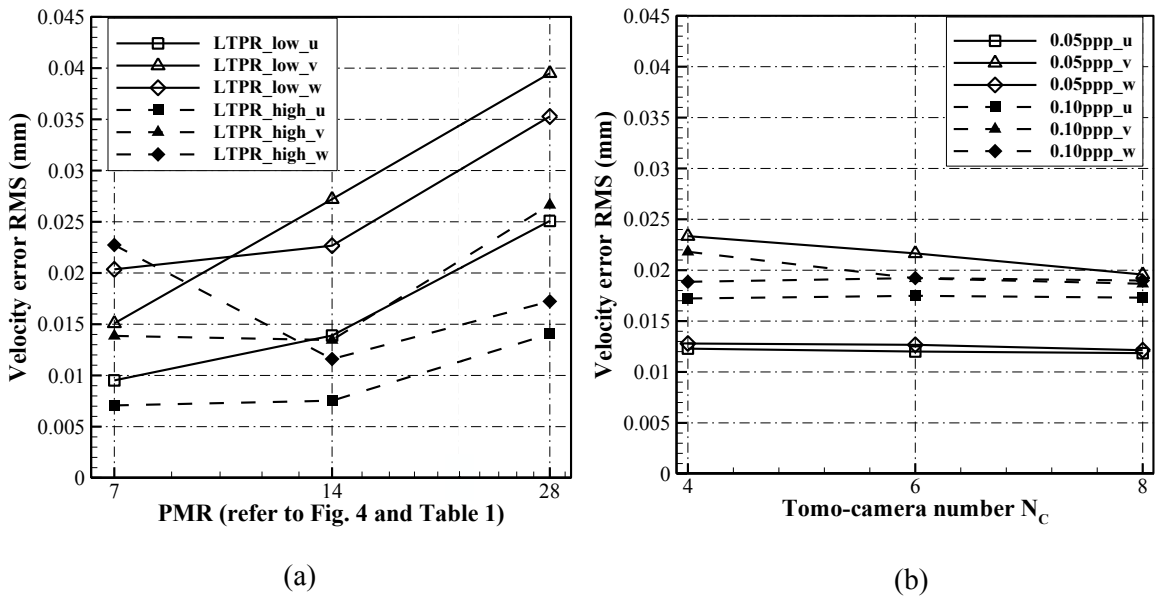


Fig. 8 Simulation results for (a) LF-PIV for the low (LTPR=3.13, 4.17, 6.25) and high resolution (LTPR=12.5, 16.67, 25) light-field cameras
(b) Tomo-PIV (pixel size=0.075mm)

3 Experimental Tests

Simulation studies in section 2 demonstrate the key parameters that influence the relative performance of LF-PIV and Tomo-PIV, however do not take into account the effects of background noise, lens distortion, misalignment between tomographic cameras as well as misalignment between MLA and image sensor in a light-field camera. To conduct a direct comparison, the LF-PIV and Tomo-PIV experimental

1 systems are used to perform simultaneous measurements on the same volume of a low-
2 speed jet flow. A schematic of the experimental setup is presented in Fig. 9, which
3 shows that the sensor plane of the LF-PIV is parallel to the jet direction and the four
4 tomographic cameras are positioned in a cross-like configuration.
5
6
7
8
9

10
11 The flow scenario was produced by a recirculating pump and a $D=20\text{mm}$ circular
12 nozzle. Reynolds number tested was $Re_D = 2000$ and the measurement volume was
13 approximately $1.9 D \times 1.3 D \times 0.5 D$ along the x -, y -, z -directions and located at about
14 $2.25 D$ above the nozzle exit. Tracer particles were uniformly seeded in the water tank
15 (Dantec Dynamics $20 \mu\text{m}$, $\rho = 1.03 \text{ g/cm}^3$ polyamide seeding particles), which
16 resulted a seeding density of 0.062ppp for Tomo-PIV and 0.06ppm for LF-PIV. Note
17 that such density is optimal for Tomo-PIV and slightly sparse for LF-PIV.
18
19
20
21
22
23
24
25
26
27
28

29 Illumination were provided by a 10mm thick laser sheet (Beamtech double pulse Nd:
30 YAG laser, 200 mJ/pulse , 532 nm). Readers are referred to Shi et al. (2017) for more
31 details on the experiment setup. Light-field particle images were captured by an in-
32 house light-field camera (equipped with a Micro-NIKKOR 200mm lens), which was
33 developed from a 29M pixel Imperx B6640 PIV camera (Shi et al. 2016).
34
35
36
37
38
39
40

41 Tomographic particle images were captured by four 4M pixel Imperx B2014 PIV
42 cameras (each equipped with a Micro-NIKKOR 85mm Scheimpflug lens). The five
43 cameras were synchronized via a pulse generator and connected to the host computer
44 (Dell Precision T7910) via four EPIX PIXCI E4 frame grabbers. To measure the
45 phase-averaged flow field, a 1Hz perturbation was introduced into the flow delivery
46 pipe before the settling chamber, where it was synchronized with the five cameras and
47 the laser pulse.
48
49
50
51
52
53
54
55
56
57
58
59
60
61
62
63
64
65

1 To facilitate the comparison of these two techniques, 20 instantaneous light-field and
2 tomographic particle image pairs were captured. The effective resolution of light-field
3 camera and tomographic cameras used in this experiment are 6600×4400 pixel² and
4 480×320 pixel², respectively, which results in a LTPR=47.27. The light-field particle
5 images were reconstructed with the DRT-MART method (400 iterations), and the
6 tomographic particle images were sequentially processed with the self-volume
7 calibration (Wieneke 2008) and 40 iterations MLOS-SMART method (Atkinson and
8 Soria 2009). For light-field particle image reconstruction, the pixel voxel ratio was set
9 as 2:2:10 in x-, y- and z-direction, which results in a reconstruction domain of
10 $3300 \times 2200 \times 182$ voxels. For Tomo-PIV reconstruction, the pixel voxel ratio
11 maintained at 1:1 for all directions, which results in a reconstruction domain of
12 $480 \times 320 \times 130$ voxels. It should be noted that, although a light-field camera with a high
13 pixel resolution produces a high-resolution reconstruction in the image plane, owing
14 to limited angular resolution of single light-field camera, such high pixel resolution
15 does not result in a higher depth resolution (z-direction in this case) than the Tomo-
16 PIV. After particle intensity field reconstruction, instantaneous velocity fields were
17 calculated with a three-dimensional multi-grid cross correlation algorithm with 75%
18 overlap. Initial and final interrogation windows are $320 \times 320 \times 64$ voxels, 160×160
19 $\times 32$ voxels for LF-PIV, and $64 \times 64 \times 64$ voxel, $32 \times 32 \times 32$ voxel for Tomo-PIV.
20 Despite the difference in reconstruction resolution, the non-dimensionalised final
21 interrogation window size for LF-PIV and Tomo-PIV is $0.092D \times 0.095D \times 0.088D$ and
22 $0.13D \times 0.13D \times 0.12D$ respectively. To summarise, key experimental parameters are
23 listed in the table below.

Table 4 Reconstruction and interrogation parameters used for experimental image processing

| | LF-PIV | Tomo-PIV |
|---|-------------------|-------------------|
| Camera Number | 1 | 4 |
| Effective resolution of each camera | 6600×4400 | 480×320 |
| Field of View (mm³) | 38×26×10 | |
| p_p | 0.0058mm/pixel | 0.079mm/pixel |
| Particle density | 0.06ppm | 0.062ppp |
| MLA resolution | 450×350 | - |
| LTPR | 47.27 | - |
| PMR | 14 | - |
| Pixel voxel ratio | 2:2:10 | 1:1:1 |
| Reconstruction resolution (voxel) | 3300×2200×182 | 480×320×130 |
| Voxel size (mm) | 0.012×0.012×0.055 | 0.079×0.079×0.079 |
| 1st interrogation window size (voxel) | 320×320×64 | 64×64×64 |
| 2nd interrogation window size (voxel) | 160×160×32 | 32×32×32 |
| Spatial resolution (mm³) | 1.84×1.84×1.76 | 2.53×2.53×2.53 |
| Vector number | 79×51×19 | 57×37×13 |

Any spurious vectors, which was 4.1% for LF-PIV and 5.2% for Tomo-PIV, were conservatively validated by 3×3×3 median filter and replaced with linear interpolation.

1 Reconstruction and cross-correlation process were both accelerated by a NVIDIA
2 TITAN X GPU unit, which took 4.5hrs for LF-PIV reconstruction, and 10.7s for
3 Tomo-PIV reconstruction. The phase-averaged jet flow fields as measured by LF-PIV
4 and Tomo-PIV are presented in Fig. 10, which shows the vorticity contour together
5 with velocity vectors (colours represent the velocity component in the jet direction).
6
7 Both LF-PIV and Tomo-PIV are shown to successfully capture the vortex roll-up
8 along the jet shear layer, with the overall flow structure looking similar between the
9 two techniques. By performing a cross-correlation between these two flow fields, the
10 correlation coefficient was 0.94, indicating a high level of agreement between the LF-
11 PIV and Tomo-PIV results.
12
13
14
15
16
17
18
19
20
21
22
23
24
25
26
27
28
29
30
31
32
33
34
35
36
37
38
39
40
41
42
43
44
45
46
47
48
49
50
51
52
53
54
55
56
57
58
59
60
61
62
63
64
65

1
2
3
4
5
6
7
8
9
10
11
12
13
14
15
16
17
18
19
20
21
22
23
24
25
26
27
28
29
30
31
32
33
34
35
36
37
38
39
40
41
42
43
44
45
46
47
48
49
50
51
52
53
54
55
56
57
58
59
60
61
62
63
64
65

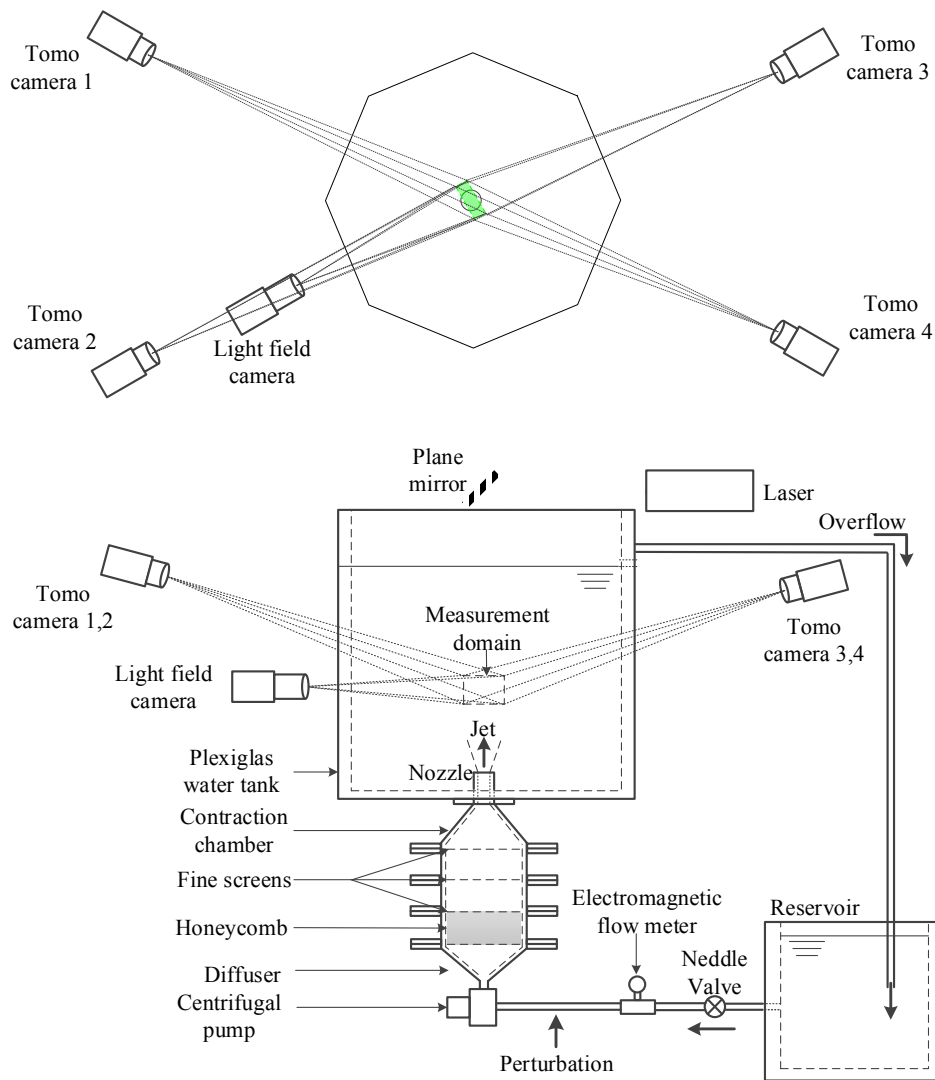


Fig. 9 Schematics of the low-speed jet flow experimental setup

1
2
3
4
5
6
7
8
9
10
11
12
13
14
15
16
17
18
19
20
21
22
23
24
25
26
27
28
29
30
31
32
33
34
35
36
37
38
39
40
41
42
43
44
45
46
47
48
49
50
51
52
53
54
55
56
57
58
59
60
61
62
63
64
65

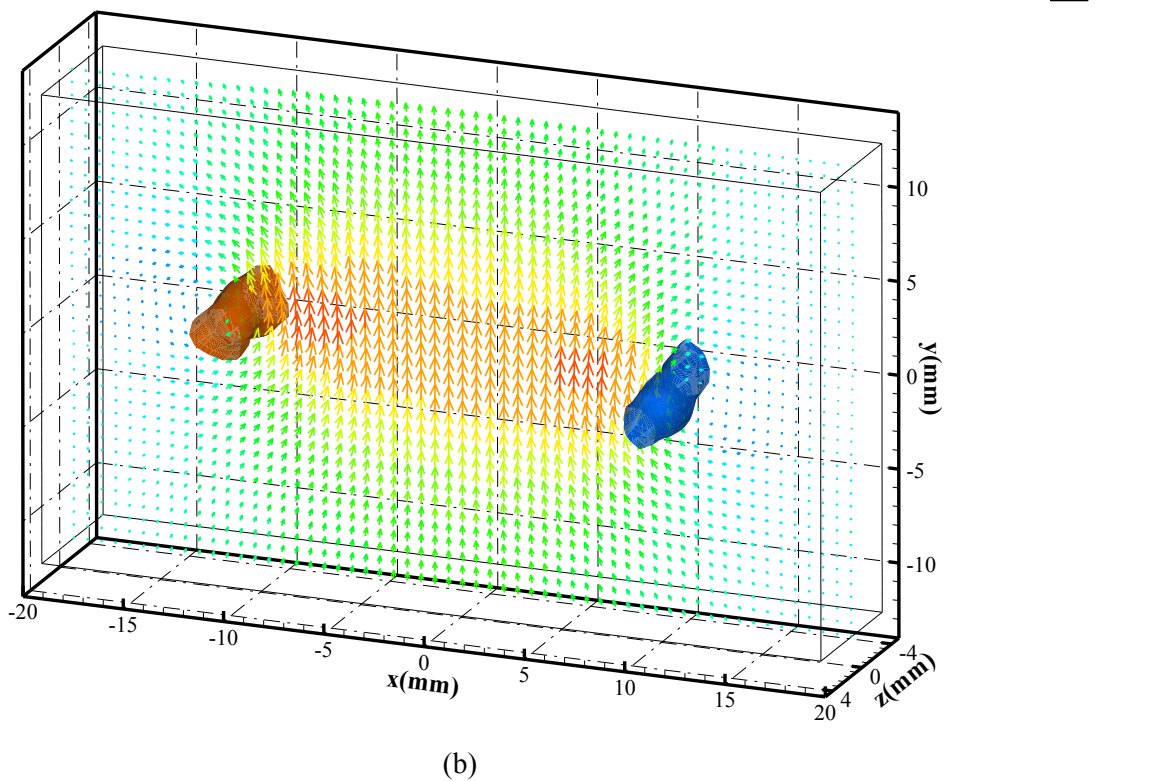
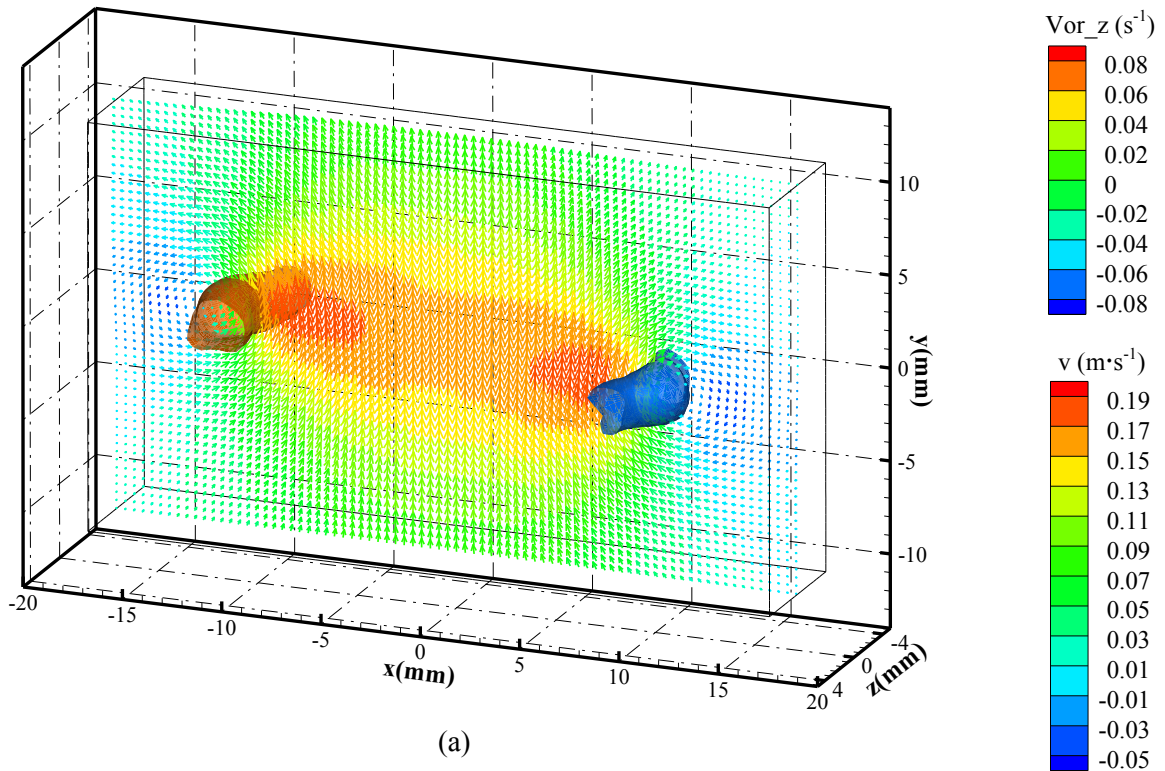


Fig. 10 Phase-averaged jet flow field measured by (a) LF-PIV and (b) Tomo-PIV

4 Conclusions

A direct comparison between the single-camera Light-Field Particle Image Velocimetry (LF-PIV) and multi-camera Tomographic Particle Image Velocimetry (Tomo-PIV) was carried out in the current study. Comparisons were performed using both synthetic light-field and tomographic particle images as well as experimental images of a round jet flow. Results demonstrate that the single-camera LF-PIV can achieve accuracy equivalent to or better than that of the multi-camera Tomo-PIV for the same field of view, but doing so requires a relatively high PMR and LTPR. While for the same total number of pixels, single-camera LF-PIV cannot match the seeding density or spatial resolution of Tomo-PIV due to its smaller angular resolution. The present comparative study between the novel single-camera LF-PIV and traditional multi-camera Tomo-PIV points out the significant potential of such single-camera based volumetric velocity measurement technique, owing to its greater simplicity of the experimental setup and the ability to provide accurate 3C-3D flows measurements even in applications where optical access is limited.

Acknowledgements

Financial support provided by National Natural Science Foundation of China (Grant No. 11472175), Shanghai Raising Star Program (Grant No. 15QA1402400) and Singapore Ministry of Education AcRF Tier-2 grant (Grant No. MOE2014-T2-1-002) are gratefully acknowledged. The support of Australian Research Council (ARC) for this work is gratefully acknowledged, Dr. Atkinson was supported by an ARC Discovery Early Career Researcher Award (DECRA) fellowship while undertaking this work.

References

1
2 Adrian RJ (1984) Scattering particle characteristics and their effect on pulsed laser
3
4 measurements of fluid flow: speckle velocimetry vs. particle image velocimetry.

5
6
7 Applied Optics 23:1690–1691

8
9
10 Adrian R, Westerweel J (2011) Particle Image Velocimetry. Cambridge University
11
12 Press

13
14 Belden J, Truscott T, Axiak M, Techet A (2010) Three-dimensional synthetic aperture
15
16 particle image velocimetry. Meas Sci Technol 21: 1-21

17
18
19 Atkinson C, Soria J (2009) An efficient simultaneous reconstruction technique for
20
21 tomographic particle image velocimetry. Exp Fluid 47: 553-568

22
23
24 Ding J, Wang J, Liu Y, Shi S (2015) Dense Ray Tracing Based Reconstruction
25
26 Algorithm for Light-field Volumetric Particle Image Velocimetry. 7th Australian
27
28 Conference on Laser Diagnostics in Fluid Mechanics and Combustion. Melbourne,
29
30 Australia

31
32
33
34 Elsinga G, Scarano F, Wieneke B, van Oudheusden B (2006) Tomographic particle
35
36 image velocimetry. Exp Fluid 41: 933–947

37
38
39 Fahringer T, Lynch K, Thurow B (2015) Volumetric particle image velocimetry with
40
41 a single plenoptic camera. Meas Sci Technol 26:115201

42
43
44 Georgiev T, Intwala C. Light-field camera design for integral view photography.
45
46 Adobe Tech Report, 2003

47
48
49 Georgiev T, Zheng K, Curless B, Salesin D, Nayar S, and Intwala C. Spatio-Angular
50
51 Resolution Trade off in Integral Photography. Eurographics Symposium on Rendering,
52
53 2006

54
55
56 Hinsch K (2002) Holographic particle image velocimetry. Meas Sci Technol 13: R61–
57
58 R72

- 1
2
3
4
5
6
7
8
9
10
11
12
13
14
15
16
17
18
19
20
21
22
23
24
25
26
27
28
29
30
31
32
33
34
35
36
37
38
39
40
41
42
43
44
45
46
47
48
49
50
51
52
53
54
55
56
57
58
59
60
61
62
63
64
65
- Levoy M, Hanrahan P. Light field rendering. *ACM Trans. Graph.*, 1996, 31–42
- Lumsdaine A, Georgiev T. The focused plenoptic camera. In *Computational Photography (ICCP)*, 2009 IEEE International Conference on. 2009
- Li H, Ding J, Zhao Z, Qu W, Xiong J, Shi S. (2017) Investigation of 3D flow behaviour inside a 3×3 rod bundle using Light Field-PIV and the matched refractive index techniques. *The 12th International Symposium on Particle Image Velocimetry*. Busan, Korea
- Meng H, Pan G, Pu Y, Woodward S (2004) Holographic particle image velocimetry from film to digital recording. *Meas Sci Technol* 15: 673–685
- Ng R, Levoy M, Bredif M, Duval G, Horowitz M, Hanrahan P. Light Field Photography with a Hand-Held Plenoptic Camera, tech. report CTSR 2005-02, Stanford University, 2005.
- Pereira F, Gharib M, Dabiri D, Modarress M (2000) Defocusing PIV: a three-component 3-D PIV measurement technique application to bubbly flows. *Exp Fluid* 29: S78–84
- Palafox P, Oldfield M, LaGraff J, Jones T (2008) PIV maps of tip leakage and secondary flow fields on a low-speed turbine blade cascade with moving end wall. *J Turbomach* 130: 011001
- Scarano F (2013) Tomographic PIV: principles and practice. *Meas Sci Technol* 26: 1-28
- Schanz D, Gesemann, S, Schröder A (2016) Shake-The-Box: Lagrangian particle tracking at high particle image densities. *Exp Fluid* 57: 70
- Shi S, Wang J, Ding J, Zhao Z, New TH (2016) Parametric study on light-field volumetric particle image velocimetry. *Flow Meas Instrum* 49: 70-88

1 Shi S, Ding J, New TH, Soria J (2017) Light-field camera-based 3D volumetric
2 particle image velocimetry with dense ray tracing reconstruction technique. Exp
3 Fluids 58:78
4
5

6
7 Tsai RY (1986) An efficient and accurate camera calibration technique for 3D
8 machine vision. In: Proceedings of IEEE conference on computer vision and pattern
9 recognition, Miami Beach, FL, USA, pp 364–374
10
11

12
13
14 Westerweel J, Scarano F (2005) Universal outlier detection for PIV data. Exp Fluid 39:
15 1096-1100
16
17

18
19 Wernet M, Van Zante D, Strazisar T, John W, Prahst P (2005) Characterization of the
20 tip clearance flow in an axial compressor using 3-D digital PIV. Exp Fluid 39: 743-
21 753
22
23
24

25
26 Wieneke B (2008) Volume self-calibration for 3D particle image velocimetry. Exp
27 Fluid 45: 549-556
28
29

30
31 Xu S, Ding J, Zhao Z, Atkinson C, Soria J, Shi S. (2017) 3D flow measurements of
32 circular air jet at $Re=30,000$ using light field particle image velocimetry. The 12th
33 International Symposium on Particle Image Velocimetry. Busan, Korea
34
35
36
37
38
39
40
41
42
43
44
45
46
47
48
49
50
51
52
53
54
55
56
57
58
59
60
61
62
63
64
65